Electrically-functionalised nanoindenter dedicated to local capacitive measurements: experimental set-up and data-processing procedure for quantitative analysis

Solène Comby-Dassonneville, Fabien Volpi, Marc Verdier

Electrically-functionalised nanoindenter dedicated to local capacitive measurements: experimental set-up and data-processing procedure for quantitative analysis

Solène Comby-Dassonneville, Fabien Volpi, Marc Verdier

Univ. Grenoble Alpes, CNRS, Grenoble INP, SIMaP, 38000 Grenoble, France

Corresponding author: fabien.volpi@simap.grenoble-inp.fr

Declarations of interest: none

Abstract

In this work, we report the experimental development and the application of a new characterisation tool combining mechanical testing and dielectric characterisation. The experimental set-up is essentially a nanoindentation head functionalised for capacitive measurements. First the experimental procedure for the characterisation of dielectric thin films is given: detailed set-up description, procedure for the capacitance-vs-voltage (C-V) measurements, stray capacitance,... Secondly, a complete data-processing method is proposed to perform the quantitative analysis of capacitance data. To this end, a fully analytical model has been developed, able to relate the C-V curves to the system characteristics (set-up geometry and specimen properties) without any fitting parameter. Finally dielectric films with different thicknesses and relative permittivities have been tested to validate both the characterisation tool and the data-processing method. The analytical model has been used to predict the permittivity of each dielectric thin film. The extracted data have been compared to data obtained from a calibrated macro-scale technique and showed remarkable agreement. One of the strengths of the data-processing method is to eliminate the stray capacitance which usually disturbs local capacitance measurements. Even though the effect of mechanical load is not investigated in the present study, the experimental proof-of-principle is shown and the data-processing method is validated. This work opens prospects for local and quantitative dielectric characterisations under

mechanical loads. It should also fill a gap between quantitative characterisations at macro-scales and spatially highly-resolved characterisations at nano-scale.

Key words: Functional nanoindentation; Local capacitance measurement; Stray capacitance; Quantitative data-processing

Highlights:

- A new set-up combining mechanical and dielectric local characterisations is described
- The set-up is a nanoindentation head functionalised for capacitive measurements
- A complete data-processing method is proposed to perform quantitative analysis
- The procedure eliminates the effect of stray capacitance before quantitative analysis
- The method is successfully applied to the characterisation of model dielectric films

1. Introduction

The development of small-scale characterisation techniques of dielectric structures has become increasingly critical for various application fields: micro- and nano-electronics [1, 2], electronics [3], electrochemistry [4, 5], photovoltaics [6], biological science [7],… Traditionally this can be achieved through the coupling of Atomic Force Microscopes (AFM) [8] to capacitance sensors (or more generally to impedance-meters [9, 10]). After the pioneering work of Matey and Blanc [11], the early Scanning Capacitance Microscopes (SCM) that combined AFM to capacitive measurements were dedicated to surface topography mapping [12, 13]. These set-ups have then been extended to the profiling of dopant distribution in semiconductors [1, 14-16], which remains the major application for SCM. In these systems, the capacitance sensor is an inductance-capacitance-resistance (LCR) resonator operating at ultra-high frequency (usually 915 MHz) coupled to a peak detection circuit. The tip-to-sample capacitance $C_{Tip-to-Sample}$ being part of the LCR circuit, any change in its value is sensed from a change in resonance, further related to dopant concentration. Even though SCM is currently applied to the characterisation of Metal-Insulator-Semiconductor (MIS) structures, this technique does not apply to dielectric film characterisation as there is no voltage-dependent depletion in such materials. A pioneering attempt [17] to perform permittivity and alternating conductivity measurements on dielectric materials was spatially-limited by the large scale probe (circa 100 µm). Nanoscale Impedance Microscopy (NIM) has then been developed to characterize frequency-dependent charge transport and polarization mechanisms in dielectric films [3, 4, 10, 18-20]. Contrary to SCM, the NIM technique provides the measurement of both resistance and capacitance of the tip-to-sample interface: both the amplitude and phase of the current induced by an alternating bias are measured.

However one of the main limitations for the quantitative analysis of either SCM or NIM data is the stray capacitance due to the electrostatic interaction between the sample and various parts of the AFM (tip cone, cantilever and probe holder [21, 22]). Thus the signal of interest (capacitance between the tip apex and the sample) needs to be distinguished from the stray capacitance that can be several orders of magnitude larger (typically 100-500 fF against 1 fF). It has been shown that this stray capacitance is strongly influenced by AFM scanning conditions [23]. Several attempts have been made to remove this stray capacitance from raw data. For instance Lee et al [23] report the use of a bucking circuit to subtract an adjustable capacitance to the measured

admittance. Even though this approach allows high sensitivity measurements, the exact value of the stray capacitance is unknown. Schneegans et al have worked on minimizing the stray capacitance by shielding and biasing the tip holder [22]. The same team proposed a dual-scan procedure to remove environmental effects [24]. Extensive calibration processes based on analytical or numerical modelling have also been developed to obtain quantitative capacitive measurements [20-22].

In parallel to the development of these AFM-based tools, the development of nanoindentation testing has been driven by the need for mechanical characterizations of small-scale systems [25-27]. Capacitive transducers are widely used in nanoindentation systems [28-30] but they are only used as gauges to monitor the indenter column displacement. This approach has been further extended to capacitance measurements at the sample level but the measurement of tip-to-sample capacitance has essentially been used to monitor sample deformation [31, 32]. However the coupling of capacitive measurements to nanoindentation tests has been rarely used for the characterisation of dielectric properties of materials. To our knowledge, the only study reporting capacitance measurements on dielectrics through an indenter tip can be found in [33]: this study focuses on the dielectric relaxation processes induced by mechanical loading of piezoelectric thin films and the relationship with charge defect generations during loading. However, no quantitative analysis of the absolute capacitance and/or of the stray capacitance is reported.

The present paper first reports the development of a tool able to combine mechanical testing and dielectric characterisation. This set-up is essentially a nanoindentation head that has been functionalised for capacitive measurements. Secondly, a data-processing method is proposed to eliminate the effect of the stray capacitance before the quantitative analysis of the capacitive signal. Even though the effect of mechanical load is not investigated in the present study, the experimental proof-of-principle is shown and the data-processing method is validated on model dielectric thin films. On these films, dielectric permittivity is quantitatively extracted and compared to reference a macro-scale characterisation method.

2. Experimental details

2.1 *Instrumentation*

The present set-up combines different commercial instruments, with customized adapter systems. Fig. 1 shows a Computer-Aided Design (CAD) drawing of the set-up.

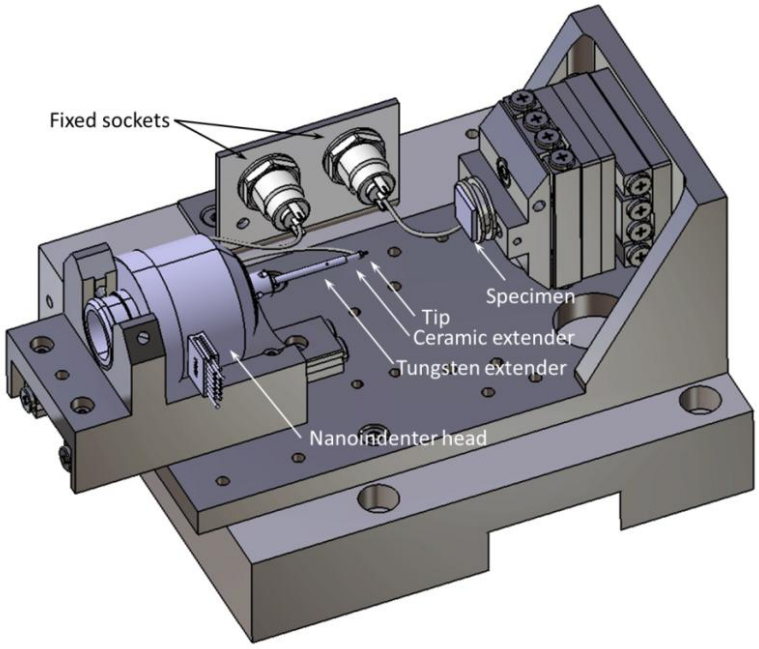

Figure 1: CAD drawing of the set-up.

The nanoindentation head is a commercial actuator (InForce 50 actuator from Nanomechanics Inc), displaying a maximum load of 50mN and a static load resolution at the µN. The tip was a 5µm-large boron-doped diamond (BDD) flat-punch tip (truncated cone geometry with 30° opening angle). From an electrical point of view, this tip displays a metal-like behavior. In the present study, the tip was not used to penetrate plastically within the specimen but only to position the electrical probe on top of the dielectric surface, thus building up a MIS structure. The effect of the application of a mechanical load will be shown elsewhere. The tip is screwed on a 3 mm-long ceramic extension, which is screwed on a 1.5 cm-long tungsten extender. The ceramic part is necessary to insulate the conductive tip from the grounded extender. Electrical contacts are made with thin copper wires connected to fixed sockets.

Actuator and sample displacements are performed with linear positioners from SmarAct GmbH. Typical travel ranges are at the cm scale with a ~1 nm resolution. The set-up presented in this

paper has three translation axes: one axis translates the actuator along the indentation axis (referred as Z-axis), and two axes were dedicated to sample positioning (referred as X and Y axes). The overall stiffness of the instrument frame has been checked by indenting fused-silica specimen. Stiffness larger than 10^6 N/m has been extracted, thus validating the mechanical behavior of the overall set-up (including the different parts and workpieces along the indenting axis).

Impedance measurements were performed with an E4980A LCR-meter from Agilent with sensitivity better than 1 nS for admittance measures at 2MHz. A 'parallel model' was used for data post-processing (capacitance in parallel with a conductance). For all tests, the parallel leakage conductance was shown to be negligible compared to the capacitance of interest (i.e. the admittance phase angle was between 88 and 90°). A white LED was used to expose the MIS stack to light in order to force the semiconductor inversion regime. LED exposure avoids any heating issues which would be detrimental to nanoindentation testing.

2.2 Samples

As already stated, the present study aims at validating both the experimental set-up and the quantitative data-processing method. Thus only model materials (with well-controlled characteristics) are presented here: thin silica films deposited on silicon substrates. At this stage of the set-up validation, specimens with mm-scale homogeneity are required in order to compare the local measures (performed with this set-up) with the measures performed on a calibrated technique (Hg-probe system [34]) that operates at the mm-scale. Substrates were n-doped silicon, with donor content of ~$6.5.10^{14}$ cm^{-3} (extracted by 4–point probe resistive measurements). Substrates have been cleaned with Piranha solution (H_2SO_4 + H_20_2) before silica growth. Silica films have been deposited in two steps:

- A first dry thermal oxidation has been performed on all specimens to grow a first 49 nm silica layer (by silicon consumption). This oxidation process has been performed for 20min at 1050°C under O_2 flow. This first oxide layer ensures an optimal Si/SiO_2 interface with low defect density.
- An extra silica layer has been further deposited by Plasma Enhanced Chemical Vapor Deposition (PECVD) over this thermal oxide. This film has been deposited at 280°C under SiH_2, N_2O and Ar flows. Different thicknesses have been deposited (Table 1).

Total silica thickness has been measured by ellipsometry, while dielectric relative permittivity has been measured on a calibrated Hg-probe system.

Sample	Thermal silica thickness (nm)	PECVD silica thickness (nm)	Total silica thickness (nm)	Permittivity (Hg-probe)
A	49	0	49	3.5 (+/-0.1)
B	49	108	157	4.7 (+/-0.2)
C	49	135	184	4.4 (+/-0.2)
D	49	432	481	5.4 (+/-0.2)
E	49	925	974	5.2 (+/-0.2)

Table 1: Specimen description.

3. Electrical behaviour of Metal-Insulator-Semiconductor structures

In our approach, the quantitative analysis of capacitance measurements relies on the analysis of MIS capacitive behaviour. Thus a short description of MIS diagrams and the related capacitances under applied voltage is given here (a more complete description can be found in [35]).

Let us consider a MIS structure (area S) subjected to a quasi-static electrical bias V_{DC} (the reference potential is taken on the metal terminal (Fig. 2)). Sweeping V_{DC} from negative to positive voltage forces the structure to switch from accumulation to inversion regimes, which are the two extreme possible configurations for a MIS structure.

- In the accumulation regime (Fig. 3(a)), electrons from the n-type substrate are accumulated at the insulator/semiconductor interface. As a result the MIS capacitance C_{MIS}^{Acc} equals the insulator capacitance C_{Ins} and can be described by Eq. (1), with ε_{Ins} and t_{Ins} the insulator relative permittivity and thickness, respectively.

$$C_{MIS}^{Acc} = C_{Ins} = \frac{\varepsilon_0 \varepsilon_{Ins} S}{t_{Ins}} \qquad (1)$$

- In inversion regime (Fig. 3(b)), the band bending within the semiconductor is strong enough to stabilize minority carriers (holes) at the insulator/semiconductor interface. Locally, the semiconductor has the properties of a p-type semiconductor. This inversion layer is thermodynamically stable, but might require external stimulus to be generated (light exposure in the present case). At high frequency (present case), once this inversion layer is set, the extension of the depletion region is fixed to its maximal value W_{Max}. W_{Max} can be expressed by Eq. (2), with ε_{SC} the semiconductor relative permittivity, kT

the thermal energy (in J), N_D the donor density and n_i the intrinsic carrier concentration. In this inversion regime, the MIS capacitance C_{MIS}^{Inv} is due to two capacitances in series (C_{Ins} and C_{Dep}), which are both constant (Eq. (3)).

$$W_{Max} = \sqrt{\frac{4\varepsilon_0 \varepsilon_{SC} kTln(N_D/n_i)}{e^2 N_D}} \qquad (2)$$

$$C_{MIS}^{Inv} = \left(\frac{1}{C_{Ins}} + \frac{1}{C_{Dep}}\right)^{-1} = \left(\frac{t_{Ins}}{\varepsilon_0 \varepsilon_{Ins} S} + \frac{W_{Max}}{\varepsilon_0 \varepsilon_{SC} S}\right)^{-1} \qquad (3)$$

In both regimes, the capacitance C_{Exp} which is experimentally measured is the sum of the MIS capacitance (either C_{MIS}^{Acc} or C_{MIS}^{Inv}) with the stray capacitance C_{Stray} which is unknown (Eq. (4)).

$$C_{Exp} = C_{MIS}^{Acc\ or\ Inv} + C_{Stray} \qquad (4)$$

Finally the Capacitance-versus-Voltage curve (C-V) presents an S-shape as shown in Fig. 3. Both extreme levels correspond to the accumulation and inversion regimes. If the stray capacitance is independent of the applied voltage, the curve span ΔC (see figure) is only driven by the material properties (insulator thickness, permittivities of insulator and semiconductor, doping level,…). In that case, ΔC is given by Eq. (5).

$$\Delta C = C_{MIS}^{Acc} - C_{MIS}^{Inv} \qquad (5)$$

Only this ΔC span will be further used in the upcoming quantitative analysis. One can notice that the stray capacitance is automatically withdrawn by working on this differential magnitude. This analytical method eliminates the stray capacitance without any fitting parameter or extensive set-up calibration (to be compared to the works reported for instance in [20-22]), and should be suitable for the analysis of capacitance-measures acquired on any system subjected to a stray capacitance that is voltage-independent.

Within the frame of this simple analytical model (where the 'parallel plate capacitor' model can be used) the $\Delta C_{Analytic}^{Parallel}$ span of C-V curve is simply obtained by subtracting Eq. (1) and Eq. (3), thus leading to Eq. (6).

$$\Delta C_{Analytic}^{Parallel} = C_{Ins} - \frac{C_{Ins} \cdot C_{Dep}}{C_{Ins} + C_{Dep}} = \frac{C_{Ins}}{1 + C_{Dep}/C_{Ins}} \qquad (6)$$

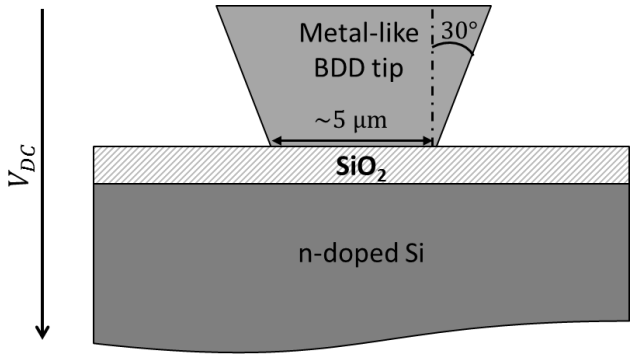

Figure 2: Schematic of the MIS stack, with parallel plates.

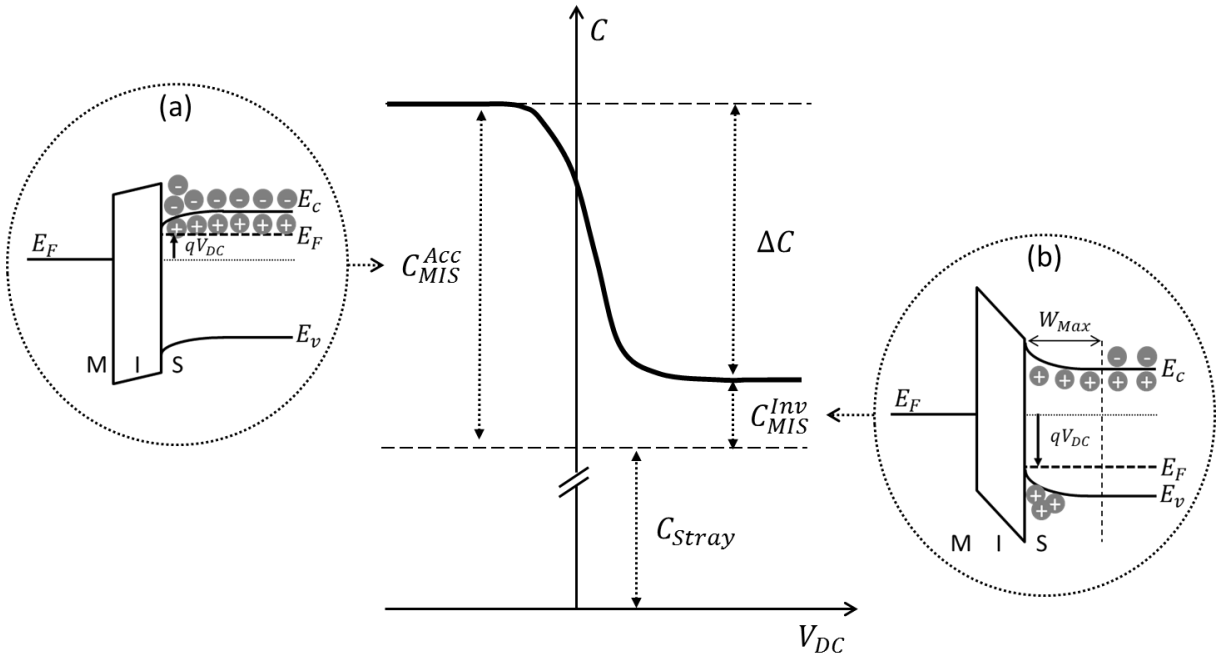

Figure 3: Typical C-V curve with the corresponding band diagrams in accumulation (a) and inversion (b) regimes.

4. Experimental

4.1 *Set-up geometry : electrode area and angular misalignment*

The quantitative analysis of capacitance requires the precise knowledge of different magnitudes defining the set-up geometry: the electrode area S and the angular misalignment α (Fig. 4).
As already stated, the probe used in this study was a flat-punch tip, i.e. a truncated cone (Fig. 2). As a first approximation, only the flat top part of the tip is considered. The corresponding area has been extracted from an AFM mapping of the tip. The electrode radius R has been measured to lie between 2.3 and 2.4 µm (i.e. smaller than the expected nominal 2.5 µm). For further details, refer to Supplementary material, Supp.Mat.1.
Because of unavoidable misalignments of the workpieces constituting the set-up, an intrinsic angular misalignment α builds-up between the flat-punch and specimen surfaces (Fig. 4). This angle has been measured experimentally by two independent methods (see Supplementary material, Supp.Mat.2). It lies within 0.0096 and 0.012 rad. This value circa 0.01 rad is rather standard for nanoindentation systems [36].

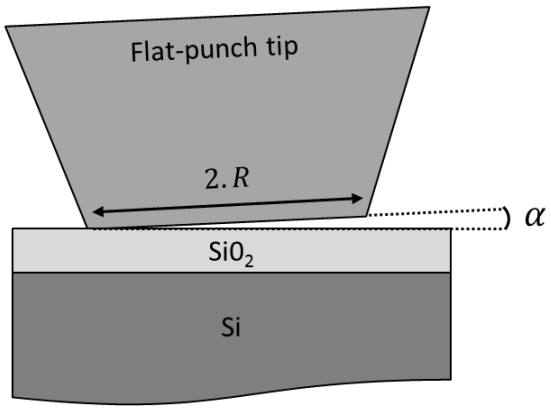

Figure 4: Schematic of the MIS stack with angular misalignment.

4.2 Mechanical contact with the specimen for capacitive measurements

The first step of the capacitive measurement procedure is to set the flat-punch tip into contact with the specimen surface. Once the specimen surface is reached by automated approach, the nanoindenter head is set into a force-controlled mode to maintain contact with the surface. The typical pressure applied to the sample during capacitive measurements was 100kPa, thus keeping material deformation into its elastic domain (no tip penetration within the specimen, no film

degradation by plastic indentation). The effect of mechanical load on material properties is not investigated in the present paper.

4.3 Capacitive measurements

For all capacitive measurements reported in the present article, the oscillating voltage level V_{AC} and the test frequency f have been set to 2.5 V and 2MHz, respectively. Before each C-V monitoring, the MIS structure was initially set into inversion regime by applying a large positive V_{DC}^{Inv} bias and by exposing it to light for 5 s. Then measurements were performed for V_{DC} bias going back and forth from V_{DC}^{Inv} (inversion regime) to V_{DC}^{Inv} (accumulation regime), with a 1 V step. Between each successive capacitance measure the inversion layer was regenerated by polarising the sample at V_{DC}^{Inv}. A schematic of this "pulsed" procedure is given in Fig. 5. The pulse duration was set to 1 s. Each capacitance measure lasted for ~ 5s. V_{DC}^{Inv} and V_{DC}^{Acc} voltages were optimized for each specimen.

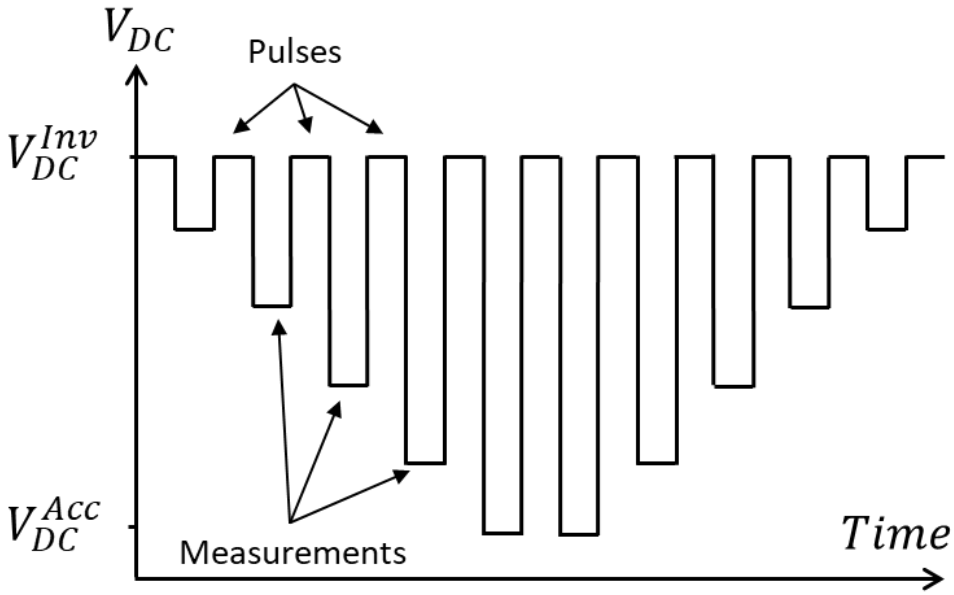

Figure 5: Voltage chronogram for a full C-V measurement.

4.4 Stray capacitance

One of the motivations for the development of capacitive-nanoindentation was to control the stray capacitance. In typical NIM or SCM experiments, the contributions to the stray capacitance are local and they strongly depend on the probe position on the specimen [21-23]. These

contributions (i) depend on the mechanical load [22,23] and (ii) come mostly from the tip-to-sample vicinity, involving the asymmetric influence of the AFM cantilever geometry. With a nanoindenter, the probe geometry is fixed and is highly symmetrical close to the specimen (Fig. 6). The asymmetrical parts of the probe contribute to the stray capacitance at a macroscopic scale which smooths the sensitivity to surface topography or chemistry. Consequently, the stray capacitance is expected to be voltage-independent (i.e. identical in accumulation and inversion regimes) and constant over large areas, which enables its subtraction without any data loss.

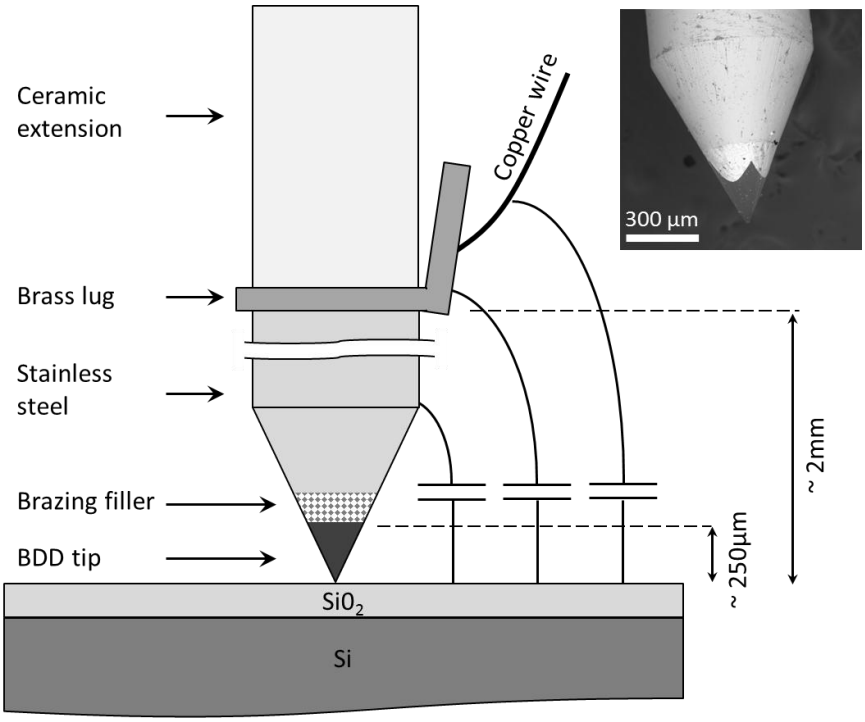

Figure 6: Schematic of the set-up in close vicinity of tip-to-sample contact. The corresponding capacitive couplings are also shown. Top right: Scanning Electron Microscope view of the tip.

5. Experiments

5.1 C-V curves

Typical C-V curves obtained on the 5 silica specimens are shown in Fig. 7. On these graphs, a capacitance offset C_{Offset} has been subtracted for graphical reading convenience. This offset lies around 220-240 fF (Table 2). The dispersion on this offset has been calculated from measures performed on several spots recorded 50 µm apart from each other. This dispersion lies below 0.1 fF for most specimens, leading to a relative dispersion $\delta C_{Offset}/C_{Offset}$ lower than 0.05%. This low dispersion confirms the low sensitivity of the system to the local tip environment. The larger dispersion observed on sample (E) must be due to macroscopic set-up modifications between experiments (probably involving motions of the copper wires (Fig. 6)). The spans of C-V curves (ΔC_{Exp}) have also been extracted (Table 2). Typical dispersion on ΔC_{Exp} is 0.03 fF, which is the sensitivity limit of the LCR-meter (peak-to-peak noise on C-V curves).

Fig 7 also paves the way to defining a figure-of-merit for dielectric films to be characterized with this system. The threshold condition is essentially driven by the ability of the LCR-meter to sense the capacitance change ΔC from accumulation to inversion regimes. It is interesting to note that sample E is close to this threshold condition, as the S-shape curve is hardly discriminated on this sample. According to Eq. 6, at first order, ΔC is proportional to C_{Ins} (which is proportional to $\varepsilon_{Ins}/t_{Ins}$ according to Eq. 1). Thus a relevant figure-of-merit could be the ratio ε_r/t (with ε_r the film permittivity and t the film thickness). For sample E, this ratio is close to 4 µm^{-1}. Therefore, this system should apply to the characterization of any dielectric film that fulfills the condition: $\varepsilon_r/t \gtrsim 4\ \mu m^{-1}$.

Sample	Total silica thickness (nm)	ΔC_{Exp} (fF)	C_{Offset} (fF)	δC_{Offset} (fF) (from site to site)	$\frac{\delta C_{Offset}}{C_{Offset}}$	$\Delta C_{Analytic}^{Parallel}$ (fF)	$\Delta C_{Analytic}^{Corrected}$ (fF)
A	49	3.49 (+/- 0.04)	232.1	0.03	0.01 %	9.51	3.28
B	157	1.72 (+/- 0.03)	225.8	0.07	0.03 %	3.34	1.72
C	184	1.52 (+/- 0.03)	238.5	0.09	0.04 %	2.48	1.4
D	481	0.55 (+/- 0.03)	238.5	0.08	0.03 %	0.86	0.61
E	974	0.20 (+/- 0.03)	224.5	2.06	0.92 %	0.27	0.22

Table 2: Experimental data extracted from C-V curves (+ ΔC spans calculated from both models).

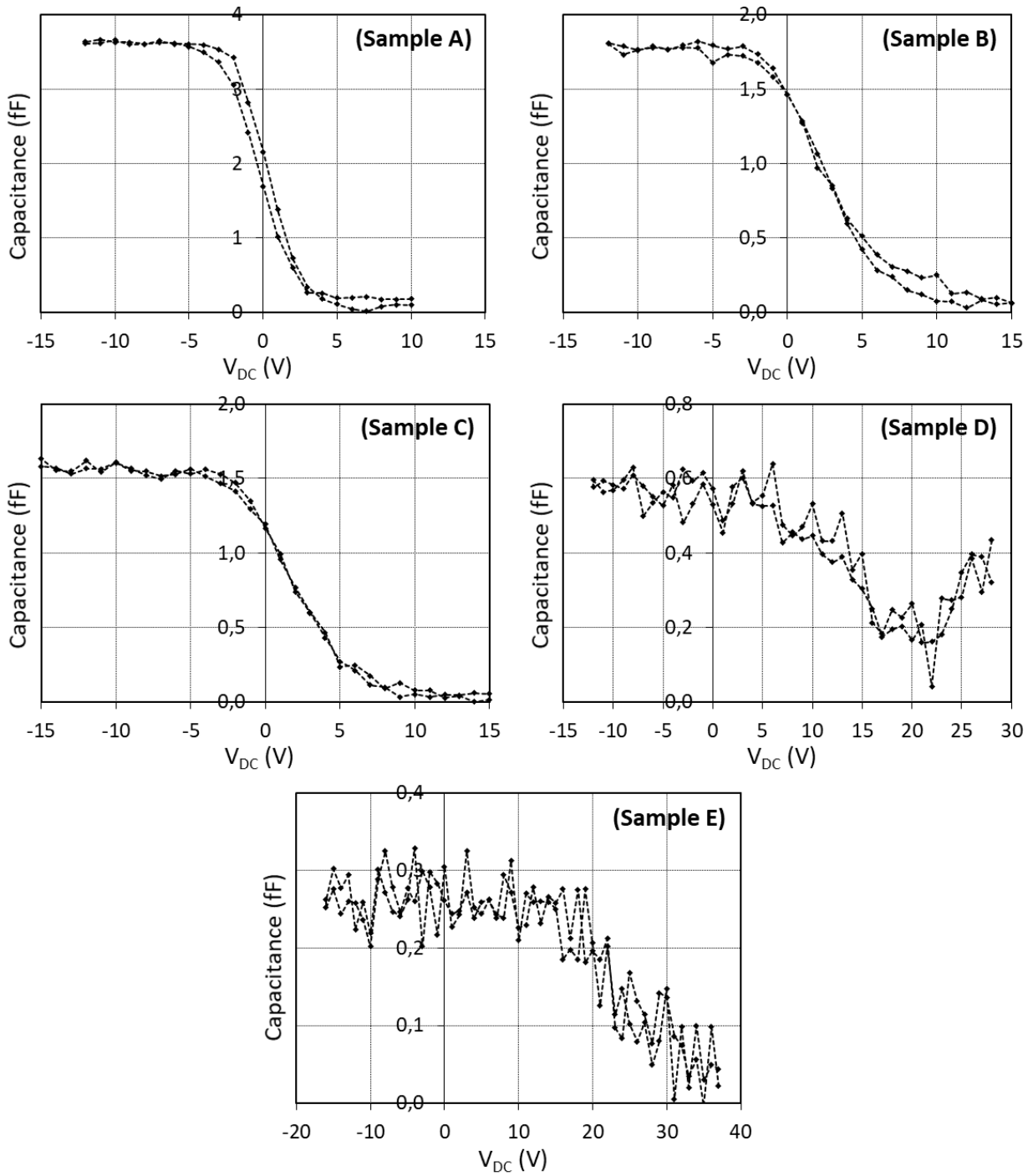

Figure 7: Typical C-V profiles recorded on samples A, B, C, D and E.

The dependence of ΔC_{Exp} on the oxide thickness is shown in Fig. 8. ΔC_{Exp} data are then compared to the simple 'parallel' model developed earlier ($\Delta C_{Analytic}^{Parallel}$ from Eq. (6)). To do so, the specimen characteristics (permittivity and thickness, reported in Table 1) have been used as inputs into the model. As it can be seen in Fig. 8, these $\Delta C_{Analytic}^{Parallel}$ data are in rather good agreement for the thickest silica film, but they strongly differ as the films get thinner (numerical data can be found in Table 2). This discrepancy actually originates from the misalignment issue discussed in the "Experimental" section. The angular misalignment between the flat-punch tip and specimen surfaces induces an air wedge (Fig. 4) that affects the capacitance measurement. With a misalignment circa 0.01 rad, the 5 µm-wide flat-tip leaves a ~50 nm air gap at its open end. Even though this air gap is negligible for the thickest films (974nm), it gets comparable to the oxide thickness on the thinnest silica films (49nm). In the following section, we propose to correct the capacitance measurement from the presence of this air wedge.

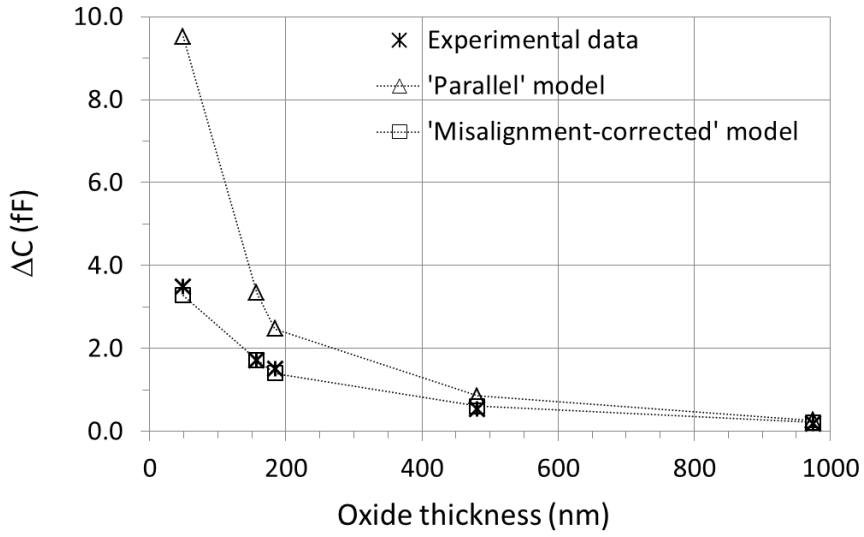

Figure 8: Evolution of ΔC_{Exp}, $\Delta C_{Analytic}^{Parallel}$ and $\Delta C_{Analytic}^{Corrected}$ with the oxide thickness.

5.2 Analytical correction of the angular misalignment

In this section the analytical model is corrected from the angular misalignment α.

5.2.1 Description of capacitance contributions

The total system capacitance is constituted of the tip-to-sample capacitance $C_{Tip-to-Sample}$ in parallel with the stray capacitance C_{Stray} (Fig. 9(a)-(b)). The tip-to-sample capacitance is constituted of elementary capacitances $dC_{Air}(x)$ (coming from the air wedge) in series with the elementary capacitances $dC_{Sample}(x)$ (coming from the tip-to-sample interaction) (Fig. 9(c)). Thus each elementary capacitance $dC_{Tip-to-Sample}(x)$ is given by Eq. (7).

$$dC_{Tip-to-Sample}(x) = \left(\frac{1}{dC_{Sample}(x)} + \frac{1}{dC_{Air}(x)}\right)^{-1} \qquad (7)$$

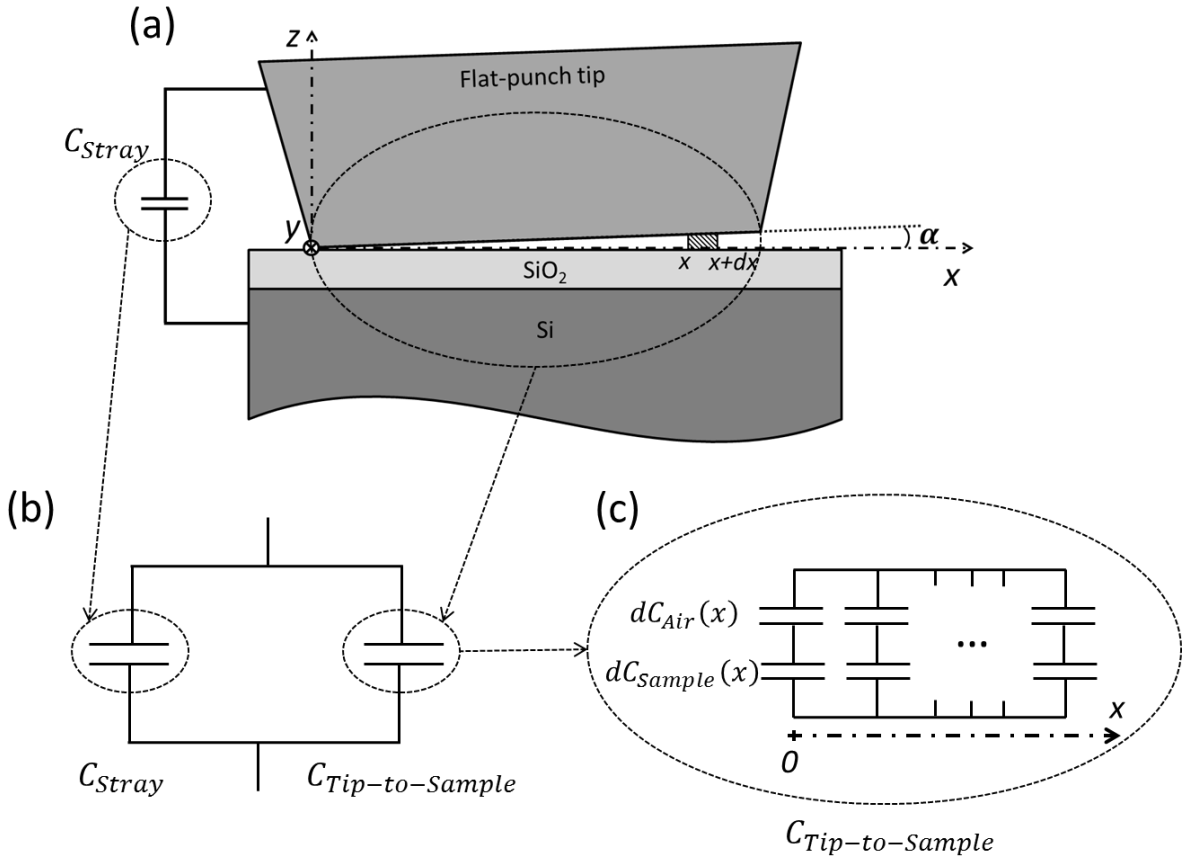

Figure 9: Capacitance modelling schematic.

5.2.2 Elementary capacitance expressions

Because the angular misalignment α is small (~0.01 rad), the plate capacitor model can be applied to these elementary capacitances (the stray field at the open-end can be neglected). Within this hypothesis, they can be expressed as follows (for coordinate references, refer to Fig. 10):

- The elementary capacitance $dC_{Sample}(x)$ is given by Eq. (8), with C_{Sample}^{S} the sample capacitance per unit area and $dS(x)$ the elementary surface area, which will be detailed later on. At this stage, C_{Sample}^{S} is generic and can account for the sample capacitance either in the accumulation regime ($C_{Sample}^{S,Acc}$) or in the inversion regime ($C_{Sample}^{S,Inv}$).

$$dC_{Sample}(x) = dS(x).C_{Sample}^{S} \qquad (8)$$

- The elementary capacitance $dC_{Air}(x)$ is given by Eq. (9), with $t(x)$ the height of the air wedge.

$$dC_{Air}(x) = \frac{\varepsilon_0 dS(x)}{t(x)} \qquad (9)$$

The surface element $dS(x)$ corresponds to the hatched sector in Fig. 10(a). $dS(x)$ can be expressed as $dS(\theta)$ in cylindrical coordinates (Eq. (10)).

$$dS(\theta) = R^2\big(1 - cos(2\theta)\big)d\theta \text{ , for } \theta \in [0;\pi] \qquad (10)$$

With R the flat-punch radius and θ the angular coordinate.

The height of the air wedge $t(x)$ corresponds to the height of the hatched sector in Fig. 10(b). Similarly, this magnitude can be expressed in cylindrical coordinates (Eq. (11)).

$$t(\theta) = R.tan(\alpha).\big(1 - cos(\theta)\big) \qquad (11)$$

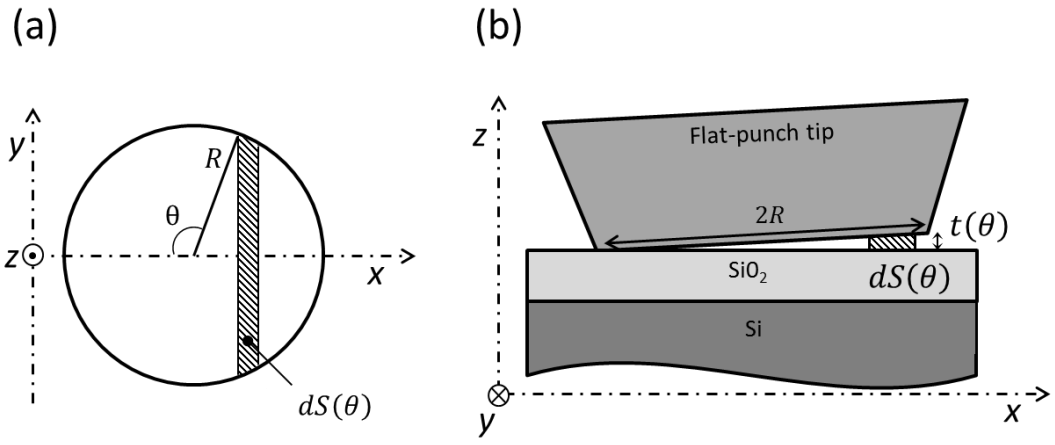

Figure 10: Air wedge geometrical descriptors: (a) plane view and (b) cross-section.

As a result, the elementary capacitance $dC_{Tip-to-Sample}$ is given by Eq. (12).

$$dC_{Tip-to-Sample}(\theta) = \frac{C_{Sample}^{S} R^2 (1-cos(2\theta))}{1+\frac{C_{Sample}^{S}}{\varepsilon_0} R.tan(\alpha).(1-cos(\theta))} d\theta \text{ , for } \theta \in [0;\pi] \qquad (12)$$

Finally the corrected tip-to-sample capacitance $C_{Tip-to-Sample}^{Corrected}$ is obtained by integrating $dC_{Tip-to-Sample}(\theta)$ over $\theta \in [0;\pi]$ (Eq. (13)) :

$$C_{Tip-to-Sample}^{Corrected} = \int_0^{\pi} \frac{C_{Sample}^{S} R^2 (1-cos(2\theta))}{1+\frac{C_{Sample}^{S}}{\varepsilon_0} R.tan(\alpha).(1-cos(\theta))} d\theta \qquad (13)$$

where $C_{Sample}^{S} = C_{Sample}^{S,Acc}$ when the MIS stack is in accumulation regime, and $C_{Sample}^{S} = C_{Sample}^{S,Inv}$ in the inversion regime. Eq. (13) can then be integrated thanks to formal computational softwares [37], thus leading to Eq. (14):

$$C_{Tip-to-Sample}^{Corrected} = \frac{2\pi\varepsilon_0^2}{C_{Sample}^{S} \cdot tan^2\alpha} \left(\frac{C_{Sample}^{S} R \tan\alpha + \varepsilon_0}{\varepsilon_0} - \sqrt{\frac{2C_{Sample}^{S} R \tan\alpha + \varepsilon_0}{\varepsilon_0}} \right) \qquad (14)$$

5.2.3 C-V curve span

As previously, the C-V curve span is the difference between the capacitances in accumulation and in inversion regimes. Once more, this difference drops the contribution of the stray capacitance, thus leading to Eq. (15):

$$\Delta C_{Analytic}^{Corrected} = C_{Tip-to-Sample}^{Corrected,Acc} - C_{Tip-to-Sample}^{Corrected,Inv} \qquad (15)$$

Similarly to the 'parallel' model, all the required inputs for this 'misalignment-corrected' model are obtained experimentally, without any fitting parameter. The corresponding data are then plotted in Fig. 8 (numerical data are given in Table 2), showing remarkable agreement with experimental data for all specimens.

5.3 Permittivity extraction

The previous section has shown that the 'misalignment-corrected' model can predict the span of C-V curves if the set-up user already knows the intrinsic film properties (thickness and permittivity). In terms of characterisation technique, this tool is rather expected to allow the extraction of intrinsic properties from experimental data. To do so, a home-made Python program has been developed to extract film permittivity from ΔC_{Exp} (a scanned value of permittivity is injected into the 'misalignment-corrected' model until the C-V spans fit). Fig. 11 reports these fitted data and compares them to permittivity values obtained on the calibrated Hg-probe system. This figure clearly shows that permittivity is efficiently predicted. The error bars have been calculated from the dispersion on tip radius, angular misalignment and the dispersion on ΔC_{Exp} (Table 2). It appears that the later (due to LCR-meter sensitivity) prevails for the thickest films while dispersion on the set-up characteristics (R and α) affects essentially the thinnest films.

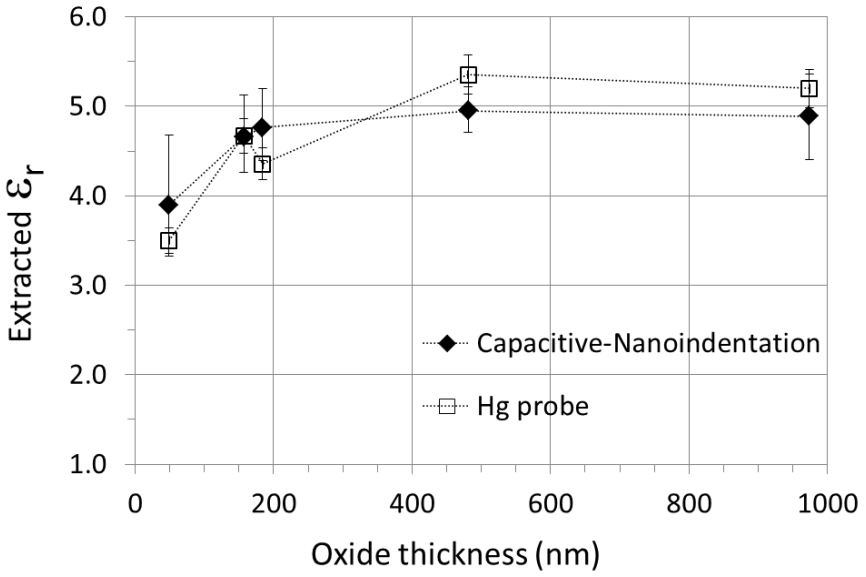

Figure 11: Relative permittivity measured on the different samples. Both techniques (capacitive-nanoindentation and Hg-probe system) are compared.

6. Conclusion

In this paper, we report the experimental development and the application of a new characterization tool made up of a nanoindentation head functionalized for capacitive measurements. First, a complete description of the system is given and a particular focus is made on the tip geometry and the angular misalignment. Then a complete data-processing method is proposed to perform quantitative analysis of the capacitance data. A fully analytical model is developed to relate the C-V curves to the system characteristics: set-up geometry and specimen properties. The proposed approach is free of adjustable parameter and should be applicable to any system with a stray capacitance that does not depend on the applied voltage. Finally, model dielectric thin films (with different thicknesses and relative permittivities) have been used to validate both the characterisation tool and the data-processing method. The extracted permittivities have been compared to a calibrated macro-scale technique and showed remarkable agreement. To our knowledge, this is the first time in literature that a quantitative analysis of the absolute capacitance is performed by using a nanoindentation head. The main strength of the whole procedure is to easily eliminate the effect of the stray capacitance which usually disturbs local capacitance measurements. Indeed, thanks to the system geometry, the stray capacitance does not depend on the applied voltage and is constant over large areas, which enables its subtraction without any data loss. Contrary to AFM-based techniques, the stray capacitance of this set-up remains unchanged when the mechanical load varies (no probe geometry change, macroscopic scale dependence), which is an advantage for the quantitative testing of load-induced dielectric phenomena. Moreover its intermediate probe size allows this tool to fill the gap between macro-scale (Hg probe) and micro-scale (SCM, NIM) techniques for the characterization of dielectric films. Even though the effect of mechanical load is not investigated in the present study, the experimental proof-of-principle is shown and the data-processing method is validated on model dielectric thin films. This work sets the stage for the quantitative investigations of materials with load-dependent dielectric properties.

Acknowledgment

This work has been performed with the financial support of the Centre of Excellence of Multifunctional Architectured Materials "CEMAM" n° ANR-10-LABX-44-01. The CEMAM program is funded by the French Agence Nationale de la Recherche (ANR).

The authors thank the technical team of SIMaP lab (Bruno Mallery, Stéphane Massucci and Nadine Vidal) for its support, as well as members of CSI/Scientec company (Les Ulis, France) for their support for the functionalisation of the nanoindentation head: Didier Pellerin, Louis Pacheco, Alan Lecoguiec and Sylvain Poulet. Finally, the authors thank François Bertin (CEA-Leti, France) for helpful suggestions in analytical integration and Guillaume Lonchampt (student Master trainee, SIMaP) for his participation to further instrument development.

References

[1] C.C. Williams, Two dimensional dopant profiling by scanning capacitance microscopy, Annu. Rev. Mater. Sci. 29 (1999) 471-504. https://doi.org/10.1146/annurev.matsci.29.1.471

[2] L.S.C. Pingree, E.F. Martin, K.R. Shull, M.C. Hersam, Nanoscale Impedance Microscopy – A characterization tool for nanoelectronic devices and circuits, IEEE Trans. Nanotechnol. 4 (2) (2005) 255-257. https://doi.org/10.1109/TNANO.2004.837856

[3] R. Shao, S.V. Kalinin, D.A. Bonnell, Local impedance imaging and spectroscopy of polycrystalline ZnO using contact atomic force microscopy, Appl. Phys. Lett. 82 (12) (2003) 1869-1871. https://doi.org/10.1063/1.1561168

[4] A. Layson, S. Gadad, D. Teeters, Resistance measurements at the nanoscale: scanning probe ac impedance spectroscopy, Electrochim. Acta 48 (14-16) (2003) 2207-2213. https://doi.org/10.1016/S0013-4686(03)00206-8

[5] R. O'Hayre, M. Lee, F.B. Prinz, S.V. Kalinin, Frequency-dependent transport imaging by scanning probe microscopy, IN Scanning Probe Microscopy : Electrical and Electromechanical Phenomena at the Nanoscale - Volume I, Springer (2007) 132-172. https://doi.org/10.1007/978-0-387-28668-6_6

[6] C.S. Jiang, C. Xiao, H.R. Moutinho, S. Johnston, M.M. Al-Jassim, X. Yang, Y. Chen, J. Ye, Imaging charge carriers in potential-induced degradation defects of c-Si solar cells by scanning capacitance microscopy, Solar Energy 162 (2018) 330-335. https://doi.org/10.1016/j.solener.2017.12.025

[7] M.C. Biagi, R. Fabregas, G. Gramse, M. Van Der Hofstadt, A. Juarez, F. Kienberger, L. Fumagalli, G. Gomila, Nanoscale electric permittivity of single bacterial cells at gigahertz frequencies by scanning microwave microscopy, ACS Nano 10 (1) (2016) 280-288. https://doi.org/10.1021/acsnano.5b04279

[8] G. Binnig, C.F. Quate, C. Gerber, Atomic force microscopy, Phys. Rev. Lett, 56 (9) (1986) 930-933. https://doi.org/10.1103/PhysRevLett.56.930

[9] J.J. Kopanski, Scanning capacitance microscopy for electrical characterization of semiconductors and dielectrics IN Scanning Probe Microscopy : Electrical and Electromechanical Phenomena at the Nanoscale - Volume I, Springer (2007) 88-112. https://doi.org/10.1007/978-0-387-28668-6_4

[10] A. Zielinski, Application of different modes of nanoscale impedance microscopy in materials research, Surf. Innov. 3 (3) (2015) 181-189. https://doi.org/10.1680/jsuin.15.00006

[11] J.R. Matey, J. Blanc, Scanning capacitance microscopy, J. Appl. Phys. 57 (5) (1985) 1437-1444. https://doi.org/10.1063/1.334506

[12] C.D. Bugg, P.J. King, Scanning capacitance microscopy, J. Phys. E: Sci. Instrum. 21 (1988) 147-151. http://doi.org/10.1088/0022-3735/21/2/003

[13] C.C. Williams, W.P. Hough, S.A. Rishton, Scanning capacitance microscopy on a 25 nm scale, Appl. Phys. Lett. 55 (2) (1989) 203-205. https://doi.org/10.1063/1.102096

[14] C.C. Williams, J. Slinkman, W.P. Hough, H.K. Wickramasinghe, Lateral dopant profiling on a 100 nm scale by scanning capacitance microscopy, J. Vac. Sci. Technol. A 8 (2) (1990) 895-898. https://doi.org/10.1116/1.576936

[15] J.J. Kopanski, J.F. Marchiando, J.R. Lowney, Scanning capacitance microscopy applied to two dimensional dopant profiling of semiconductors, Mater. Sci. Eng. B 44 (1-3) (1997) 46-51. https://doi.org/10.1016/S0921-5107(96)01797-7

[16] H. Edwards, R. McGlothlin, R. San Martin, E.U.M. Gribelyuk, R. Mahaffy, C.K. Shih, R.S List, V.A. Ukraintsev, Scanning capacitance spectroscopy: An analytical technique for pn-junction delineation in Si devices, Appl. Phys. Lett. 72 (6) (1998) 698-700. https://doi.org/10.1063/1.120849

[17] K. Asami, The scanning dielectric microscope, Meas. Sci. Technol. 5 (5) (1994) 589-592. http://doi.org/10.1088/0957-0233/5/5/020

[18] R. O'Hayre, G. Feng, W.D. Nix, F.B. Prinz, Quantitative impedance measurement using atomic force microscopy, J. Appl. Phys. 96 (6) (2004) 3540-3549. https://doi.org/10.1063/1.1778217

[19] L.S.C. Pingree, M.C. Hersam, Bridge-enhanced nanoscale impedance microscopy, Appl. Phys. Lett. 87 (23) (2005) 233117. https://doi.org/10.1063/1.2137874

[20] X. Wu, Z. Hao, D. Wu, L. Zheng, Z. Jiang, V. Ganesan, Y. Wang, K. Lai, Quantitative measurements of nanoscale permittivity and conductivity using tuning-fork-based microwave impedance microscopy, Rev. Sci. Instrum. 89 (4) (2018) 043704. https://doi.org/10.1063/1.5022997

[21] L. Fumagalli, G. Ferrari, M. Sampietro, I. Casuso, E. Martinez, J. Samitier, G. Gomila, Nanoscale capacitance imaging with attofarad resolution using ac current sensing atomic force microscopy, Nanotechnology 17 (18) (2006) 4581–4587. https://doi.org/10.1088/0957-4484/17/18/009

[22] O. Schneegans, P. Chrétien, F. Houzé, R. Meyer, Capacitance measurements on small parallel plate capacitors using nanoscale impedance microscopy, Appl. Phys. Lett. 90 (4) (2007) 043116. https://doi.org/10.1063/1.2437052

[23] D.T. Lee, J. P. Pelz, B. Bhushan, Instrumentation for direct, low frequency scanning capacitance microscopy, and analysis of position dependent stray capacitance, Rev. Sci. Instrum. 73 (10) (2002) 3525-3533. https://doi.org/10.1063/1.1505655

[24] I. Estevez, P. Chrétien, O. Schneegans, F. Houzé, Specific methodology for capacitance imaging by atomic force microscopy: A breakthrough towards an elimination of parasitic effects, Appl. Phys. Lett. 104 (8) (2014) 083108. https://doi.org/10.1063/1.4866607

[25] J.B. Pethica, R. Hutchings, W.C. Oliver, Composition and hardness profiles in ion implanted metals, Nucl. Instr. Meth. Phys. Res. 209/210 (1983) 995-1000. https://doi.org/10.1016/0167-5087(83)90911-0

[26] J.L. Loubet, J.M. Georges, J.M. Marchesini, G. Meille, Vickers indentation curves of magnesium oxide (MgO), ASME J. Tribol. 106 (1) (1984) 43-48. https://doi.org/10.1115/1.3260865

[27] J.L. Loubet, J.M. Georges, G. Meille, Microindentation techniques in materials science and engineering : Vickers indentation curves of elastoplastic materials, ASTM (1986) 72-89. https://doi.org/10.1520/STP32952S

[28] T. Motoki, S. Kiyono, T. Ono, A nanoindentation instrument for mechanical property measurement of 3d micro/nano-structured surfaces, Meas. Sci. Technol. 17 (3) (2006) 495-499. https://doi.org/10.1088/0957-0233/17/3/S06

[29] B.K. Nowakowski, D.T. Smith, S.T. Smith, L.F. Correa, R.F. Cook, Development of a precision nanoindentation platform, Rev. Sci. Instrum. 84 (7) (2013) 075110. https://doi.org/10.1063/1.4811195

[30] W. Kang, M. Merrill, J.M. Wheeler, In situ thermomechanical testing methods for micro/nano-scale materials, Nanoscale 9 (8) (2017) 2666-2688. https://doi.org/10.1039/C6NR07330A

[31] Z.L. Zhang, H. Kristiansen, J. Liu, A method for determining elastic properties of micron-sized polymer particles by using flat punch test, Comput. Mater. Sci., 39 (2) (2007) 305-314. https://doi.org/10.1016/j.commatsci.2006.06.009

[32] A. Koszewski, D. Levy, F. Souchon, Study of mechanical properties of rf mems switches by nanoindentation: characterization and modelling of electro-mechanical behavior. Sens. Actuat. A: Phys. 163 (1) (2010) 205-212. https://doi.org/10.1016/j.sna.2010.05.011

[33] V. Koval, M.J. Reece, A.J. Bushby, Relaxation processes in dielectric and electromechanical response of PZT thin films under nanoindentation, Ferroelectrics 318 (1) (2005) 55-61. https://doi.org/10.1080/00150190590966027

[34] D.K. Schroder, Semiconductor Material and Device Characterization, Third Edition, John Wiley & Sons (2006). https://doi.org/10.1002/0471749095

[35] E.H. Nicollian, J.R. Brews, MOS (Metal Oxide Semiconductor) Physics and Technology, John Wiley & Sons (1982). http://doi.org/10.1116/1.571867

[36] N.B. Shahjahan, Z. Hu, Effects of angular misalignment on material property characterization by nanoindentation with a cylindrical flat-tip indenter, J. Mater. Research 32 (8) (2017) 1456-1465. https://doi.org/10.1557/jmr.2016.478

[37] WolframAlpha, from https://www.wolframalpha.com/ (last accessed November 7, 2018).